nature communications

Article

https://doi.org/10.1038/s41467-024-55569-0

Revealing the excited-state mechanisms of the polymorphs of a hot exciton material

Received: 31 May 2024

Accepted: 11 December 2024

Published online: 02 January 2025

Check for updates

Ziqi Deng[1], Chao Huang[1], Yunfeng Luo[1], Jiaxing He[1], Lan Li[1], Xinyu Pang[2], Guanheng Huang[1] & David Lee Phillips[1]

As the investigation of high efficiency thermally activated delayed fluorescence (TADF) materials become more mature, regulating the emission properties for single organic luminescence molecules has gained increasing interest recently. Herein, the donor-acceptor compounds F-AQ comprised of fluorene and anthraquinone is reported, and it exhibits a polymorphism with muti-color emission and TADF from high-level intersystem crossing (hRISC). The photodynamics and excited-state transient species were studied by femtosecond transient absorption (fs-TA) spectroscopy. As a result, an unambiguous signal of through space charge transfer (TSCT) was observed in the fs-TA spectra of the crystal with the π-π interaction between the fluorene and anthraquinone groups, whereas the other amorphous solids and crystal only show a conventional deactivation pathway of hRISC-TADF. In this study, we successfully realize the direct observation of the morphism-dependent TSCT in a crystal, which provides the observations in solid-state ultrafast excited-state dynamics and deepens the insight into the design of potential mechanochromic materials and thermochromic utilization of the polymorphism of organic luminescence molecules.

Organic luminescence materials have played an indispensable role in a wide variety of applications, including organic light emitting diodes (OLED)[1–3], chemical/biological sensors[4–7], bioimaging probes[8–11], and anti-counterfeiting technique[12,13]. After the maturity of mechanisms for thermally activated delayed fluorescence (TADF) and the improvement of design strategy for TADF systems, a high-efficiency electroluminescent material was realized[14–17]. Traditionally, the TADF is originated from the reversed intersystem crossing (RISC) from the lowest triplet state (T_1) to the lowest singlet state (S_1). However, there exists a TADF utilizing the exciton generated from a higher triplet state (T_n) via high-level reversed intersystem crossing (hRISC). The hot exciton material can effectively utilize the triplet nonradiative exciton and realize near 100% internal quantum efficiency (IQE) in theory[18–24]. Hence, this type of material has attracted increasing interest recently. To implement hot exciton TADF, one of the key factors, the rate constant of ISC (k_{ISC}) between the singlet state and the triplet state, needs to be mentioned. Based on the equation to calculate k_{ISC}[8,25]:

$$K_{ISC}(S_n - T_n) = \frac{2\pi}{\hbar} SOCME^2 \frac{1}{\sqrt{4\pi k_B T}} \exp\left(-\frac{\Delta E_{ST}{}^2}{4\lambda k_B T}\right) \quad (1)$$

From the Eq. (1), we can figure out that two parameters will have a significant impact on the k_{ISC}, the energy level between the singlet state and triplet states (ΔE_{ST}) and the spin-orbital coupling matrix element (SOCME). The most common strategy to gain a large k_{ISC} is constructing the electron donor-acceptor system to create a charge transfer (CT) state which will significantly lower the ΔE_{ST} value, especially the through space charge transfer (TSCT)[26–31]. Compared to the through bond charge transfer (TBCT), TSCT can realize a larger extent of charge separation and thus significantly narrow ΔE_{ST}[31]. Moreover, a large enough gap between T_n and T_1 is another key factor to ensure

[1]Department of Chemistry, The University of Hong Kong, Pokfulam Road, Hong Kong 999077, China. [2]Department of Chemistry, Southern University of Science and Technology, Shenzhen 518055, China. e-mail: phillips@hku.hk

effective hRISC, because it is highly related to the rate constant of internal conversion (IC) which is a competitive process for hRSIC[32].

Apart from the efficiency enhancement, the regulation of the emission color of the organic luminescence material is also an essential task[33–35]. According to some previous reports, controlling the aggregation state of the solid is an effective method to realize the regulation, taking advantage of different intermolecular interactions or molecule conformation in polymorphs[36,37]. The formation of different polymorphs is determined by various factors, including solvent type, aggregation rate, temperature, humidity, pressure, mechanical force, and so on[37]. Thereinto, utilizing the adjustment of temperature, pressure, and mechanical force, the organic luminescence molecules have been fabricated into thermochromic material[38,39], piezochromic material[40–42], and mechanochromic material[43–46].

However, even though many polymorph TADF materials have been reported, the detailed mechanism and ultrafast processes involved for the emission in the solid state were rarely studied, especially excited-state photodynamic variation in different aggregation modes. In this study, fluorene which exhibits a hRISC property was selected as the electron donor[23,47], and anthraquinone as the electron acceptor because it presents the potential of forming different polymorphs when bonding with another moiety[37]. The 2-(9,9-dimethyl-9H-fluoren-2-yl)anthracene-9,10-dione (F-AQ) was designed, synthesized, and fabricated into different solid phases (Fig. 1a), amorphism-G (amo-G), amorphism-Y (amo-Y), crystal-YG (cry-YG), and crystal-O (cry-O), with the 1 *wt*% doped PMMA film and glass state for reference. The steady-state UV-vis absorption, photoluminescence (PL) spectroscopy and transient PL decay spectroscopy was used to study the ground-state and excited-state properties of these samples, revealing the cry-O will have the absoprtion peak with the longest wavelength and lifetime of hot exciton TADF. Moreover, the femtosecond/nanosecond transient absorption (fs/ns-TA) spectroscopy[48–50] were conducted to investigate the photodynamics and the transient species involved in the luminescence of TADF from hRISC, and a clear TSCT signal is observed for cry-O. This intriguing observation and characterization for solid-state photodynamics provides insight into the design of luminescence materials with the consideration of polymorphism-dependent behavior.

Results and discussion

The investigation of F-AQ was initiated from its spectroscopic analysis in the solution phase. From the steady-state UV-vis absorption

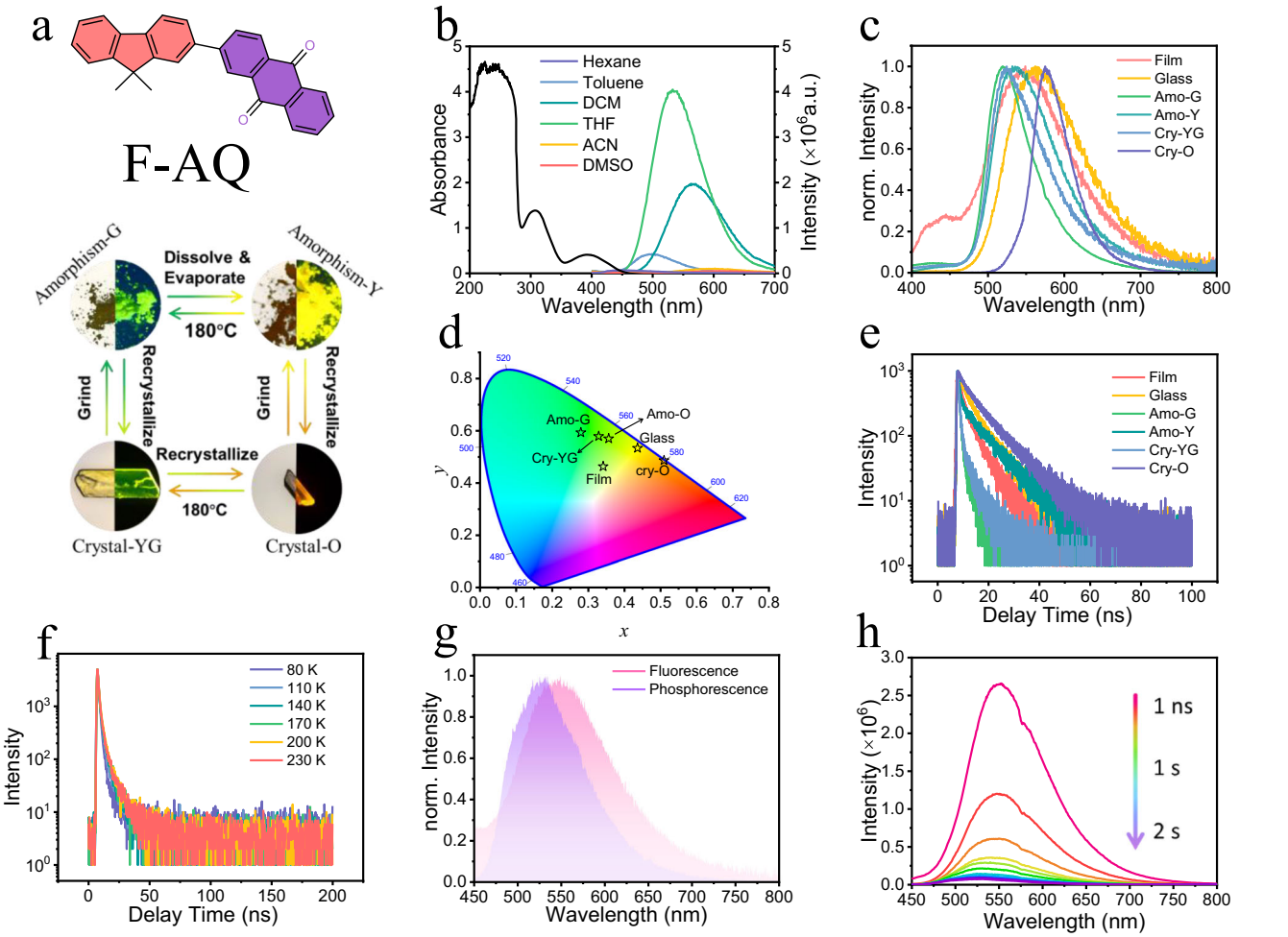

Fig. 1 | Photophysical properties of F-AQ and its different solid states. **a** Molecular structure and four different morphs of F-AQ. **b** Steady-state UV-vis absorption spectra of F-AQ solution of ACN, and steady-state PL spectra of F-AQ measured in the solvents of cyclohexane (λ_{max} = 450 nm), toluene (λ_{max} = 501 nm), dichloromethane (λ_{max} = 565 nm), tetrahydrofuran (λ_{max} = 533 nm), acetonitrile (λ_{max} = 599 nm), and dimethylsulfoxide (λ_{max} = 607 nm). **c** Steady-state PL spectra of F-AQ@PMMA film (λ_{max} = 549 nm), glass state (λ_{max} = 563 nm), amo-G (λ_{max} = 532 nm), amo-Y (λ_{max} = 538 nm), cry-YG (λ_{max} = 543 nm), and cry-O (λ_{max} = 575 nm). **d** PL decay curve of the emission maxima for F-AQ@PMMA film, glass state, amo-G, amo-Y, cry-YG, and cry-O. **e** The temperature-dependent PL decay curves of F-AQ@PMMA film from 80 K to 230 K. **f** CIE color space diagram of F-AQ@PMMA film, glass state, amo-G, amo-Y, cry-YG, and cry-O. **g** Comparison of fluorescence peak and phosphorescence peak of F-AQ@PMMA film. **h** Transient emission spectra of F-AQ@PMMA film from 1 ns to 2 s with a gate width of 200 ms.

Table 1 | Photophysical properties of F-AQ in solution, F-AQ@PMMA film, glass state, amo-G, amo-Y, cry-YG, and cry-O

	$\lambda_{em,max}$(nm)	CIE coordinate	QY	τ_F (ns)	τ_{DF} (ns)	k_F (×10 ns^{-1})	k_{DF} (×10 ns^{-1})
Solution(Tol)	501	–	0.98	0.4[c]	–	2.83	–
PMMA film	549	(0.39, 0.56)	0.13	0.98	5.20	1.02	0.19
Glass state	563	(0.44, 0.53)	< 0.10	2.32	7.92	0.43	0.13
Amo-G	532	(0.27, 0.59)	< 0.10	0.62	4.00	1.61	0.25
Amo-Y	538	(0.39, 0.57)	0.46	0.69	9.23	1.45	0.11
Cry-YG	543	(0.33, 0.58)	< 0.10	0.68	5.46	1.47	0.18
Cry-O	575	(0.51, 0.49)	0.38	2.14	9.37	0.47	0.11

[a]$\lambda_{em,max}$: the wavelength of emission maxima; [b]Φ_{FL}: fluorescence quantum yield; [c]τ_F: lifetime of prompt fluorescence; [d]τ_{DF}: lifetime of delayed fluorescence from hRISC; [e]k_F: rate constant of prompt fluorescence, $k_F = 1/\tau_F$; [f]k_{DF}: rate constant of delayed fluorescence from hRISC.

spectrum, there appears three peaks located at 390 nm, 315 nm, and 250 nm. The emission peaks of F-AQ show evident solvent effects from 450 nm to 600 nm with the increasing of the solvent polarity, indicating the existence of a CT species (Fig. 1b). The solids of F-AQ with a different aggregation state associated with F-AQ doped PMMA film were also studied by the same spectroscopy methods. As a result, the F-AQ@PMMA film shows similar features to those of the solution phase, while the aggregation solid of F-AQ shows the growth of an absorption band in the UVA and visible region in varying degrees due to intermolecular interactions (Fig. S1). The emission spectra of each solid also presents obvious distinguishing spectra with variations in color of the different morphisms. As shown in Fig. 1c and Fig. 1d, the emission maxima were located at 549 nm, 563 nm, 532 nm, 538 nm, 543 nm, and 575 nm with the CIE coordinates of (0.39, 0.56), (0.44, 0.53), (0.27, 0.59), (0.39, 0.57), (0.33, 0.58), and (0.51, 0.49) for the F-AQ@PMMA film, glass state, amo-G, amo-Y, cry-YG, and cry-O, respectively. The PL quantum yields for these samples were also measured, 0.13, 0.04, 0.06, 0.46, 0.05, and 0.38, respectively, which suggests the aggregation mode of F-AQ will vary the luminescence efficiency in different directions. The packing mode of glass state, amo-G or cry-YG will cause aggregation-induced quenching (ACQ), while the stacking of amo-Y or cry-O can enhance the intensity of emission.

Moreover, the kinetics of the emission from F-AQ and its different solid phases were investigated by time-correlated single photon counting (TCSPC) technique excited by a 375 nm picosecond diode laser. The kinetics of F-AQ in exhibits a single-exponential decay, with the time constants of 1.53 ns, 3.62 ns, and 3.62 ns in cyclohexane, DCM, and ACN, respectively.(Fig. S3). For the situation in toluene, two time constants $\tau_1 = 0.3$ ns and $\tau_2 = 1.2$ ns was found, which may originate from the LE state emission and CT state emission. From the decay curve of each solid in Fig. 1e, the amo-G, and cry-YG exhibit the shortest lifetimes, and the amo-Y, glass state, PMMA film, and the cry-O will decay slower. Based on the double-exponential fitting results, we found that the PL decay curves of all solids displayed a two-step decay. The first lifetime can be assigned to prompt fluorescence. The temperature-dependent decay curve exhibited the prolonged lifetime and the enlarged component of the second species for each solid with the increasing temperature, (Fig. 1f and Fig. S5). Moreover, considering the delayed component of different solid phases shows much shorter lifetime values compared to the traditional one (ns scale *vs.* ms scale), the longest-lived feature can be attribute to the TADF generated from the hot triplet exciton via hRISC[18–24]. Hence, the lifetimes of the prompt fluorescence (PF) and hot exciton delayed fluorescence can be concluded, the τ_{PF} = 0.98 ns, 2.32 ns, 0.62 ns, 0.69 ns, 0.68 ns, and 2.14 ns, τ_{DF} = 5.20 ns, 7.92 ns, 4.00 ns, 9.23 ns, 5.46 ns, and 9.37 ns for F-AQ@PMMA film, glass state, amo-G, amo-Y, cry-YG, and cry-O, respectively (Fig. S4 and Table 1).

To further verify that assumption of hot exciton delayed fluorescence, theoretical calculation were carried out to study the excited-state energy levels and SOCME for F-AQ in single molecule and the crystal phases (Figs. S14–S16)[51,52]. For the energy diagram of the geometry of single F-AQ molecule in the S_1 state, the exciton from the lowest singlet excited state can transition to T_1 and T_2 state with a SOCME of 0.11 cm^{-1}, and 4.14 cm^{-1}. Since the energy gap between the S_1 and T_1 state is too larger for RISC (-0.73 eV), it may originate from the higher T_2 state. For the minimal-energy geometry in the T_2 state, the RISC becomes allowed as the energy gap narrows to 0.01 eV and the SOCME = 6.04 cm^{-1} is also satisfied for the flipping of the electron spin. Furthermore, the energy gap between T_2 and T_1 is large enough (0.49 eV) to avoid "hot" exciton decay before RISC.

The comparison of the fluorescence and phosphorescence spectra of the F-AQ@PMMA film are in good agreement with the calculation results. From Fig. 1g, the phosphorescence peak located on the left side of fluorescence peak, which means the anti-Kasha phosphorescence was generated from high level triplet state. The low-temperature transient emission (TRE) spectra of F-AQ@PMMA from 1 ns to 100 ns confirmed that the PF of it located at around 549 nm (Fig. S6), and the emission peak presents a blueshift to 532 nm from 1 ns to 2 s (Fig. 1h and S7), unveiling the conversion from hot exciton TADF to the anti-Kasha phosphorescence. Similar comparisons were also carried out for different solid states, the fluorescence and phosphorescence peaks show a close value to each other (Fig. S8), which provides a satisfactory energy level for efficient hRISC. The high-lying triplet state shows a higher energy level than singlet state for F-AQ@PMMA film and amo-G, and it will make their delayed fluorescence exhibited low sensitivity to temperature (Tables S3, S4). Similar characteristics were found in amo-Y and cry-O, which may result from the small energy splitting between S_1 and T_2 (Tables S5–S7). As for the cry-YG, it will be affected by temperature to a larger extent because the energy gap of it is much larger than the other solids (Table S6).

To further reveal the intrinsic factors that affect the excited-state dynamics of F-AQ in their different aggregation-states, the crystal structures of cry-YG and cry-O were investigated by single-crystal X-ray diffraction. As the results show, the crystalline phase of cry-YG is monoclinic with space groups of C2/c, while the cry-O exhibits a triclinic phase and P-1 space groups. The selected dimers extracted from the full crystal structure of cry-YG and cry-O (Figs. S10 and S11) are shown in Fig. 2a, and the intermolecular interaction is clearly displayed for two crystals. For cry-YG, there exists an apparent π-π stacking between the acceptor anthraquinone group of two molecules with a distance of about 3.62 Å. However, the π-π stacking is observed between the acceptor anthraquinone group and the donor fluorene group in cry-O, the distance between the hexatomic ring of fluorene and anthraquinone, pentatomic ring of fluorene and anthraquinone are 3.58 Å and 3.90 Å, respectively. Moreover, the Hirshfeld surface was analyzed based on the crystal structure of cry-YG and cry-O (Fig. 2b)[53,54]. Distinct differences are presented on the surfaces of the two crystals, the interaction facing the conjugated plane of anthraquinone and fluorene in cry-O shows apparently large intensity

https://doi.org/10.1038/s41467-024-55569-0

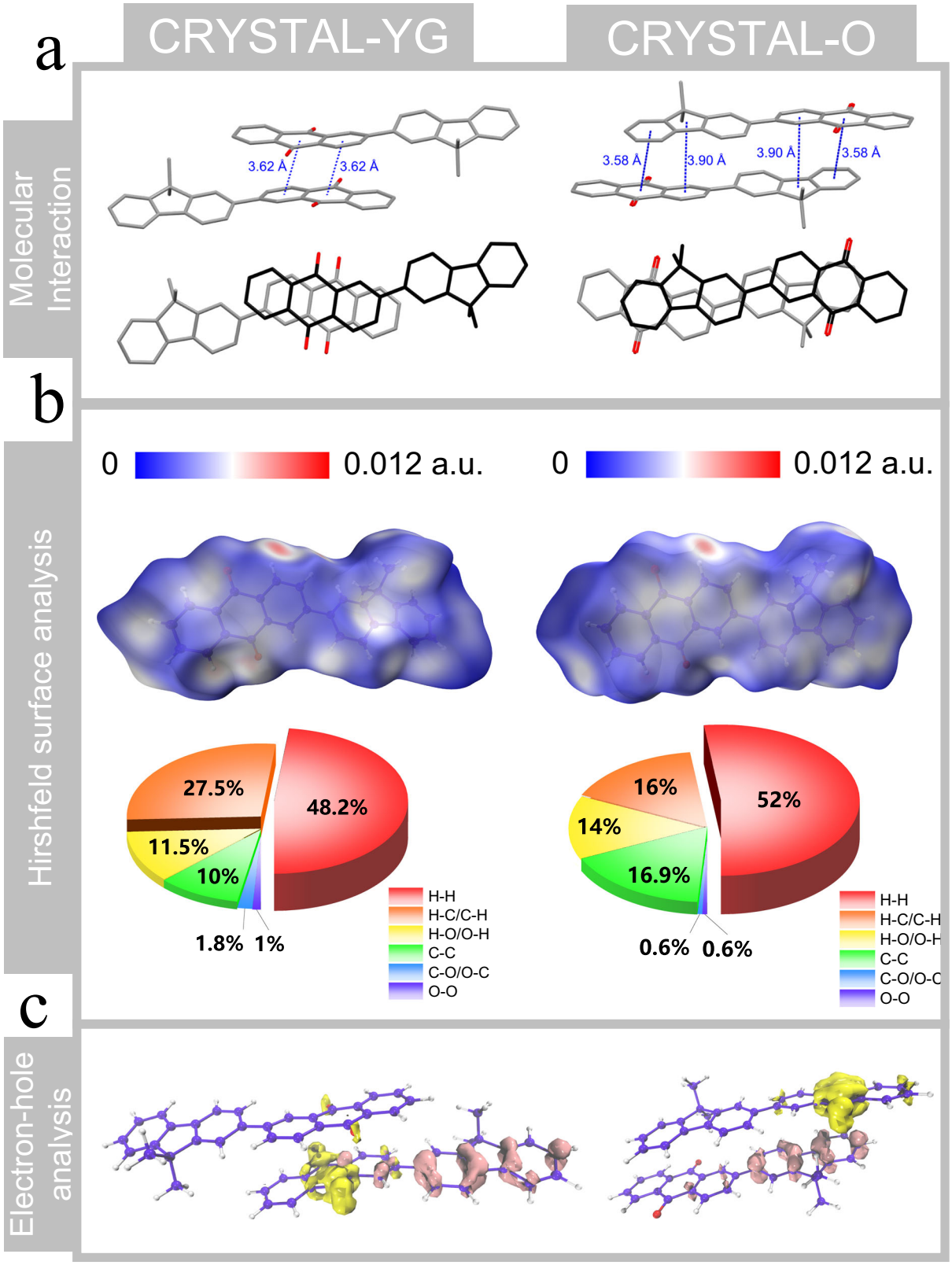

Fig. 2 | Crystal structure and analysis of cry-YG and cry-O. a Molecular interaction and overlaps of the F-AQ dimers extracted cry-YG and cry-O (Hydrogen atoms were hidden for clarity). **b** Hirshfeld surface analysis and the proportions of intermolecular H···H, C···H, O···H, C···C, C···O, and O···O and other interactions to the total intermolecular interactions based on their crystal structures. **c** Electron-hole distribution of cry-YG and cry-O (The yellow isosurface represents for electron and pink isosurface represents for hole, isovalue = 0.003).

https://doi.org/10.1038/s41467-024-55569-0

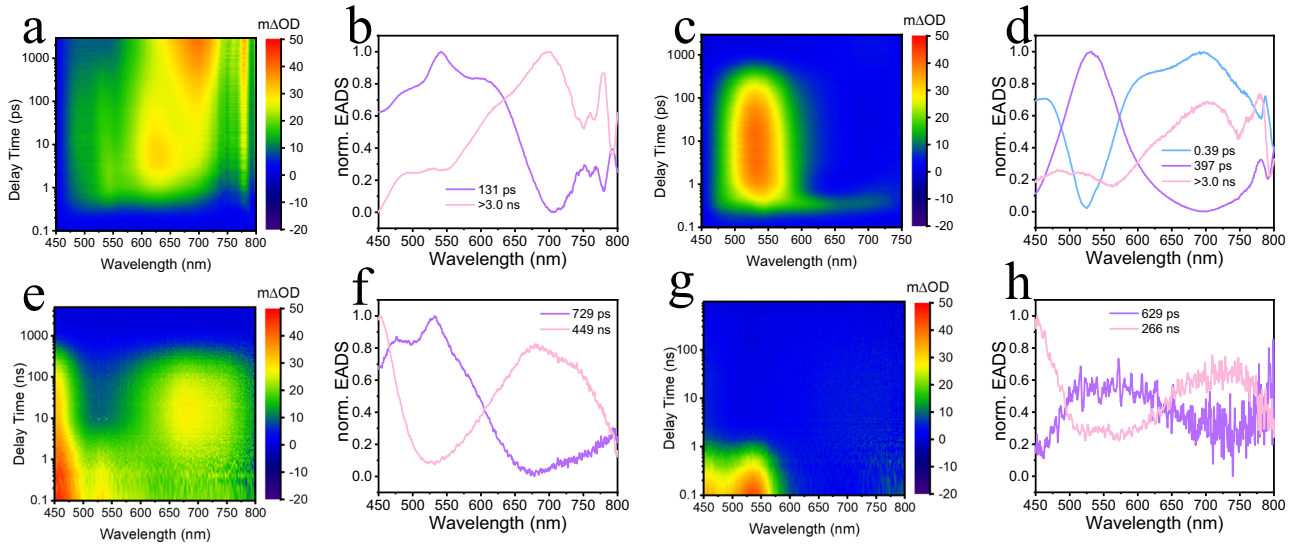

Fig. 3 | Fs-TA spectroscopy study on the F-AQ in solution. a Contour plots of fs-TA spectra for F-AQ measured in toluene; (**b**) Normalized EADS obtained from global analysis of fs-TA spectra for F-AQ measured in toluene; (**c**) Contour plots of fs-TA spectra for F-AQ measured in ACN; (**d**) Normalized EADS obtained from global analysis of fs-TA spectra for F-AQ measured in ACN; (**e**) Contour plots of ns-TA spectra for F-AQ measured in toluene; (**f**) Normalized EADS obtained from global analysis of ns-TA spectra for F-AQ measured in toluene; (**g**) Contour plots of ns-TA spectra for F-AQ measured in ACN; (**h**) Normalized EADS obtained from global analysis of ns-TA spectra for F-AQ measured in ACN.

compared to cry-YG, which is representative for the π-π interaction. Thus, from the above results, we can conclude that the cry-O can have a large possibility to proceed with a TSCT process[26,27], while the charge transfer of cry-YG may only exist intramolecularly. Moreover, the proportion of intermolecular C···C interaction is 10.0% in cry-YG, whereas this value is 16.9% cry-O (Fig. 2b), suggesting the π-π interaction is much stronger in cry-O compared to cry-YG. The electron-hole distribution of the simulated dimer of these two molecules in an excited state also supports this hypothesis (Fig. 2c). The electron (yellow) and hole (pink) are mainly distributed on the anthraquinone and fluorene in the bottom F-AQ molecule in the picture, whereas the electron is on the anthraquinone part of the upper molecule, and the hole is located on the fluorene group of the bottom F-AQ.

To obtain deeper insight into the deactivation pathway and photodynamics of the F-AQ, the fs/ns-TA spectroscopy experiments were first conducted to investigate its excited-state behaviors in the solutions with different polarity. As the results show in Fig.3, the excited state behaviors of F-AQ will be significantly affected by the polarity of environment. Based on the global analysis utilizing the sequential kinetics scheme, two evolution-associated difference spectra (EADS) species can be separated from the fs-TA spectra measured in low-polarity toluene (Fig. 3a, b), with time constants of 131 ps, and > 3.0 ns, whereas three EADS species can be obtained for the spectra measured in strongly polar ACN (Fig. 3c, d), with time constants of 0.39 ps, 397 ps, and > 3.0 ns. The first EADS species in ACN displays a broad band across 600 to 800 nm can be assigned to the local excited state (^{1}LE) species as it shows similar features to the signal observed in fs-TA spectra in nonpolar cyclohexane (Fig. S18). The second species with excited state absorption (EAS) peaked at around 550 nm is originated from the generation of charge transfer state (^{1}CT) species, as it appears simultaneously with the negative stimulated emission (SE) signal emitted from CT state. Finally, the long-lived third species at ~700 nm can be attributed to triplet state species. For the situation in toluene, the ESA signal of first species is parallel to the mix of ^{1}LE (~ 625 nm) state and ^{1}CT state (~ 550 nm), indicating an incomplete CT process in a low polar environment, and the second one is the long-lived triplet state species. Moreover, the later period excited-state dynamics is further studied by ns-TA spectroscopy (Fig. 3e–h). In ns-TA spectra, it is noted that a strong signal located at 450 – 500 nm appears within 10 ns, which may be shielded by ground state bleaching (GSB) in the fs-TA spectra. This signal is possible to be generated by the high-lying triplet state (^{3}LE), as the quick IC process from ^{3}LE to the lowest triplet state (^{3}CT) is captured in the fs-TA spectra of F-AQ measured in cyclohexane (Fig. S18b). Hence, in ns-TA spectra, the synchronous decay of ^{1}CT (~ 550 nm) and ^{3}LE (~ 470 nm) state species can be observed, revealing the equilibrium between the ISC and hRISC processes. Apart from the transition back to singlet state, the ^{3}LE state species will also decay to the lowest triplet state ^{3}CT (~ 700 nm), the ratio of these two parallel processes is greatly impacted by polarity of the environment (Figs. 3e–g).

Based on the ultrafast spectroscopic investigation in the solution phase, the solid-state photodynamics can be discussed from the analogous results of fs-TA spectroscopy. From the spectra of the F-AQ@PMMA (Fig. S20), a clear signal of conversion between ^{1}CT state and ^{3}LE state (~ 550 nm and ~470 nm) was displayed, revealing the hot exciton mechanism of F-AQ in the single-molecular state. Moreover, the glass state was used to study the general excited-state mechanism of F-AQ in an aggregated state. As a result, similar to F-AQ in toluene solution phase, the CT is not completely proceeded and there exist parallel photophysical processes. Three EADS species can be obtained from the global analysis with time constants of 6.40 ps, 182.2 ps, and >3.0 ns (Figs. 4a and 4d). The first species mainly located at 550 nm and 625 nm, which represents the formation of the ^{1}CT state and ^{1}LE state, and for the second EADS species, the ESA signal at 550 nm and 625 nm slightly decrease and the peak at 470 nm increases, indicating the generation of the ^{3}LE state. Eventually, the long-lived third species can be easily attributed to another parallel process of IC from the ^{3}LE state to the ^{3}CT state. Similarly, the three EADS species originated from the fs-TA spectra of cry-YG shows the same deactivation channel to the glass state, with time constants of 20.6 ps, 297 ps, and > 3.0 ns (Figs. 4b and 4e). The first species shows a broad band from 500 to 650 nm, which results from the signal of the ^{1}CT state and ^{1}LE state. Subsequently, the signal at around 475 nm rises and shows higher intensity than ~550 nm and ~625 nm, suggesting the generation of the ^{3}LE state, and finally the growth peak at 600 nm to 700 nm denotes the formation of the lowest ^{3}CT state. Consequently, the evolution of the ESA signal of cry-O displays an apparent difference to cry-YG. With the decay of the broadband, a new signal centered at 590 nm gradually

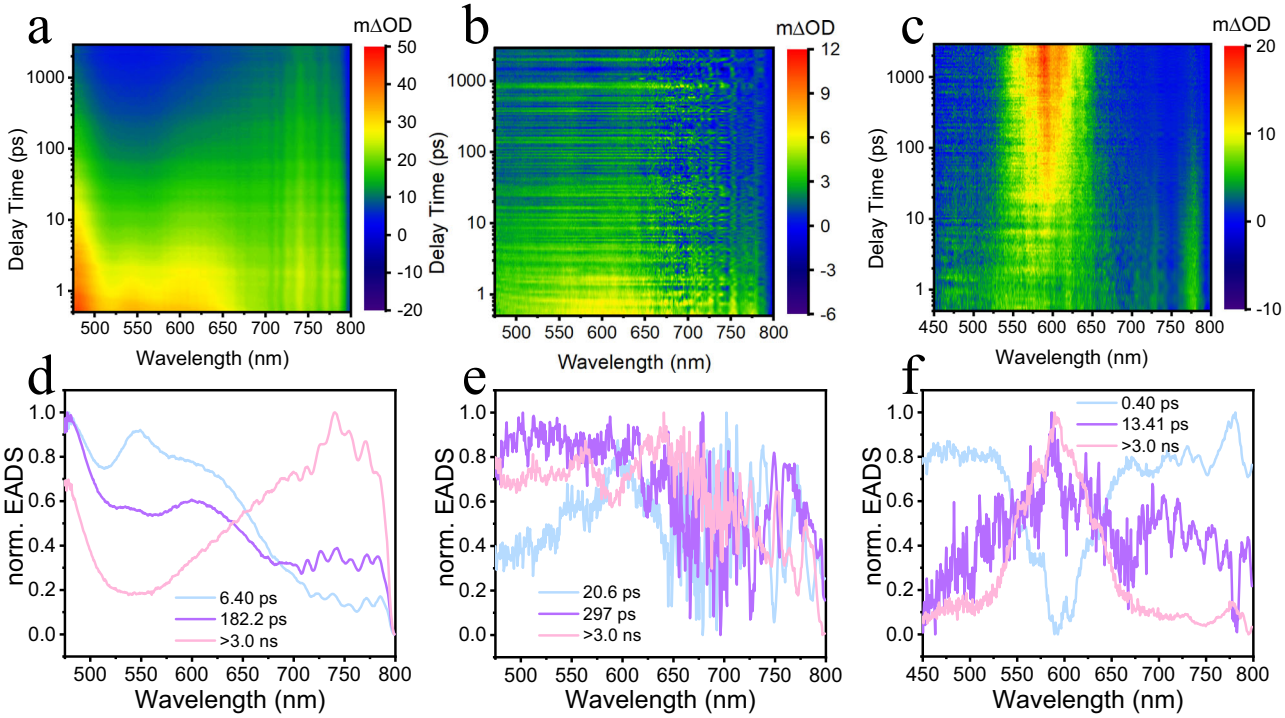

Fig. 4 | Fs-TA spectroscopy study on the F-AQ in solid states. a Contour plots of fs-TA spectra for glass state of F-AQ; (**b**) Contour plots of fs-TA spectra for glass state of Cry-YG (**c**) Contour plots of fs-TA spectra for Cry-O; (**d**) Normalized EADS obtained from global analysis of fs-TA spectra for glass state of F-AQ; (**e**) Normalized EADS obtained from global analysis of fs-TA spectra for Cry-YG; (**f**) Normalized EADS obtained from global analysis of fs-TA spectra for Cry-O.

appears and reaches a maximum at about 2 ns (Fig. 4c). This feature can be attributed to the excited-state AQ anion (Fig. S23)[55,56], indicating the intermolecular charge separation has occurred. Considering the signal of the TBCT species locates at 525 nm, we can exclude the possibility of this process. Moreover, the crystal structure analysis indicates there is a satisfactory environment for TSCT, so this slow-generated species can be assigned to the TSCT species. The global analysis revealed that three EADS species with time constants of 0.40 ps, 13.4 ps, and >3.0 ns was involved in the decay pathway of cry-O (Fig. 4f), the first species may be attributed to the generation of the ^{1}CT state and ^{1}LE state, and the second species is assigned to the TSCT process. Considering the third species shows similar features to the second one, it could be caused by the lattice relaxation of the TSCT state. Moreover, the signal ~475 nm which could be the generation of the ^{3}LE state species in the third EADS species, so this lattice relaxation process was accompanied by the ISC process simultaneously. With regard to the amorphous sample, the excited-state behaviors of amo-G and amo-Y is close as they exhibit a similar evolution of signals in their fs-TA spectra (Fig. S21 and S22). Three EADS species were separated by the global analysis, and they can be attributed to the time constants for the generation of the ^{1}CT and ^{1}LE states, the formation of the ^{3}LE state and decay from ^{3}LE state to the lowest ^{3}CT state referred to the analysis result of glass state and solution. Hence, the mechanism of the morphism-dependent TSCT process for F-AQ can be summarized in Fig. 5. The cry-YG, associated with amo-G and amo-Y, first undergo an incomplete TBCT process after excitation, and then both the ^{1}TBCT and ^{1}LE species can transition to the high-lying triplet ^{3}LE state which will transition back to the ^{1}TBCT state to emit TADF (Fig. 5b). As for cry-O, the ^{1}LE state species will generate the TSCT state taking advantage of the face-to-face arrangement between the donor and acceptor. Subsequently, the lattice relaxation of the TSCT state species occurs, followed by the ISC and hRISC to generate hot exciton TADF (Fig. 5c).

Utilizing the variation of the luminescence property in the polymorphism of F-AQ, potential applications in different functional luminescence materials, such as luminescence pigments, thermochromic material, or mechanochromic material can be realized. Utilizing the strong impact of solvent polarity on the formation of aggregated state, the F-AQ can be fabricated into two pigments with yellow and green colors, and the perforate glass plate is acted as canvas (Fig. 6a). The F-AQ solution with different solvents were carefully dropped into specific positions based on the design, and the pattern can be generated after evaporation of the solvents (Fig. 6b). Moreover, the yellow pattern "Loong" displayed in Fig. 6c was fabricated by amo-Y. After 160 °C heating for 10 min, the color of the pattern changed into green. In addition, the yellow green cry-YG can generate green amo-G, whereas orange cry-O can generate yellow *amo-Y* after grinding (Fig. S24). These two instances present the great potential of F-AQ to be fabricated into the thermochromic material and mechanochromic material.

In conclusion, we reported a polymorphism hot exciton luminescence material, and the differences in emission properties and the excited-state dynamics were investigated with a variety of spectroscopic methods. Thereinto, the cry-O which has the face-to-face stacking of acceptor anthraquinone and the donor fluorene shows a significantly longer emission lifetimes and higher quantum yields compared to cry-YG with a stacking between the anthraquinones of two F-AQ molecules. Utilizing ultrafast spectroscopy, the photodynamics of these solids were characterized. An increasing signal intensity of the excited-state anthraquinone anion was observed in the spectra of cry-O, indicating the generation of a TSCT species via intermolecular charge transfer between the packing molecules. However, the other three solid state polymorphs will not generate this species and traditionally generate hot exciton TADF similar to the situation in the solution phase. Finally, these molecules show a promising potential in the multicolor pigments, mechanochromic materials, and thermochromic materials by utilizing their polymorphism. In this work, we directly observed the morphism-dependent through-space charge transfer for one molecule and

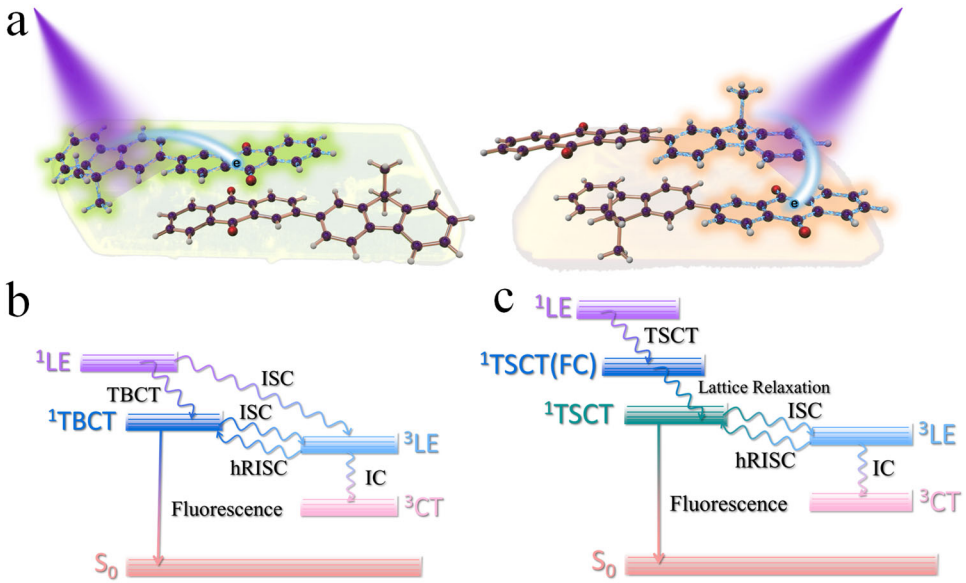

Fig. 5 | General mechanism of F-AQ in different solid states. a Schematic illustration of the different excited-state behaivours between cry-YG and cry-O. **b** Excited-state deactivation pathway of cry-YG. **c** Excited-state deactivation pathway of cry-O.

increased our knowledge of polymorphism-dependent properties of solid-state systems.

Methods

Synthesis

In a 250 ml sealed flask, 287.98 mg (1.0 mmol) of 2-bromoanthracene-9,10-dione, 285.79 mg (1.2 mmol) of (4- (9,9-dimethyl-9H-fluoren-2-yl) boronic acid, 529.90 mg(5.0 mmol) of Na_2CO_3, and 34.69 mg (0.03 mmol) of $Pd(PPh_3)_4$ were dissolved in the mixture of 20 ml THF and 2 ml H_2O. The mixture was heated to 80 °C and stirred for 12 h under the nitrogen atmosphere. After cooling to room temperature, the mixture was extracted by EA for three times. The organic layer was washed by saturated NaCl three times and dried by anhydrous Na_2SO_4. After filter and evaporation, the crude product was further purified by silica column chromatography. Orange solid was obtained in 79.8% yield.

^{1}H NMR (400 MHz, Chloroform-*d*) δ 8.61 (d, *J* = 1.9 Hz, 1H), 8.40 (d, *J* = 8.1 Hz, 1H), 8.36 (dp, *J* = 5.9, 3.5 Hz, 2H), 8.10 (dd, *J* = 8.1, 2.0 Hz, 1H), 7.88 – 7.69 (m, 6H), 7.48 (dt, *J* = 7.0, 3.0 Hz, 1H), 7.43 – 7.32 (m, 2H), 1.58 (s, 6H).

^{13}C NMR (101 MHz, $CDCl_3$) δ 183.42, 182.92, 154.63, 154.07, 147.26, 140.16, 138.36, 137.89, 134.22, 134.06, 133.91, 133.71, 133.64, 132.40, 131.96, 128.09, 127.83, 127.31, 127.24, 127.18, 126.50, 125.47, 122.73, 121.54, 120.64, 120.40, 77.34, 77.02, 76.70, 47.11, 27.19.

HRMS (QTOF-ESI) m/z $[M + H]^+$: calculated 401.1643; found 401.1530.

Preparation of the solid in different morphological state

Glass state. The glass state was prepared by melting the F-AQ in 250 °C on the surface of the quartz plate.

Amo-G. The amo-G was prepared by fast evaporation by a rotary evaporator in a saturated solution of F-AQ in DCM:ACN = 1:1.

Amo-Y. The amo-Y was prepared by fast evaporation by a rotary evaporator in a saturated solution of F-AQ in DCM:hexane = 1:1.

Cry-YG. The bulk cry-YG was prepared by slow evaporation in DCM:ACN = 1:1. The fast preparation was realized by heating the supersaturated solution of F-AQ in DCM:ACN = 1:1 to about 60 °C to saturated, and cooling down to collect the precipitated small crystal.

Cry-O. The bulk cry-O was prepared by slow evaporation in DCM:hexane = 1:1. The fast preparation was realized by heating the supersaturated solution of F-AQ in DCM:hexane = 1:1 to about 60 °C to saturated, and cooling down to collect the precipitated small crystal.

Powder X-ray diffraction

The solid sample was measured by MiniFlex 600benchtop powder X-ray diffractometer (Rigaku, Japan).

Single-crystal X-ray diffraction

Single crystal X-ray data was collected on a Bruker D8 VENTURE with Ga Kα radiation (λ = 1.34139 Å) at 100 K.

Steady-state UV-vis spectroscopy

The F-AQ were prepared into 10^{-5}M solution of ACN. The UV-vis spectra of the solution and solid sample were recorded by Cary 5000 UV-VIS-NIR spectrophotometer (Agilent, USA).

Steady-state photoluminescence spectroscopy and transient decay spectroscopy

For the solution sample, the F-AQ were prepared into 10^{-5}M solution of n-hexane, toluene, DCM, THF, ACN, and DMSO. The steady-state PL spectra and emission decay curves of the solution and solid sample were measured by FLS1000 Steady State & Time-Resolved Photoluminescence Spectrometer (Edinburgh, UK).

The steady-state PL spectra, emission decay curves, temperature-dependent PL spectra, and temperature-dependent emission decay curves of samples were also measured by FLS1000 Steady State & Time-Resolved Photoluminescence Spectrometer (Edinburgh, UK).

Phosphorescence spectroscopy

The phosphorescence spectra of the films were measured by LP920 transient absorption/emission spectrometer (Edinburgh, UK) with a 355 nm pump beam was obtained from the third harmonic output of an Nd:YAG laser. The Phosphorescence spectrum was measured with a 1-ms delayed gate.

Photoluminescence quantum yield measurement

The F-AQ were prepared into 10^{-5}M solution of toluene. The PL quantum yield of the solution and solid sample were measured by

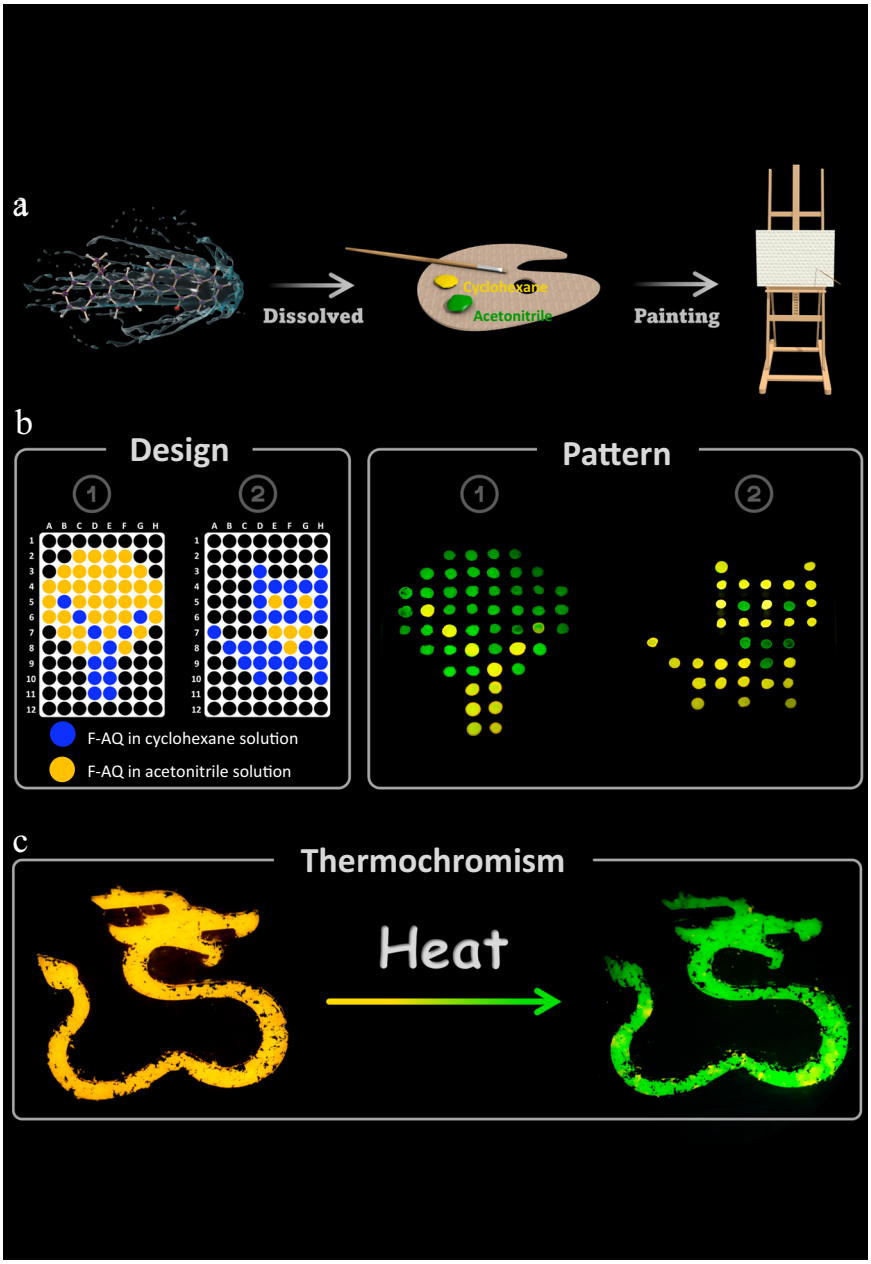

Fig. 6 | Application utilizing the polymorphism properties of F-AQ. a General procedures of preparing the pigments with different colors for painting. **b** Design and product of the pattern drawn in porous glass plates utilizing the F-AQ pigments. **c** The change in luminescence color of the "Loong" pattern fabricated by cry-O after heating to 160 °C.

Quantaurus-QY C11347-12 absolute PL quantum yield spectrometer (Hamamatsu, Japan).

Fs-TA spectroscopy

The fs-TA measurements were conducted using the Helios pump-probe transient absorption spectrometer system (Ultrafast Systems, USA) with the femtosecond laser from the Spitfire Pro regenerative amplified Ti:sapphire laser system (Spectra Physics, USA). The 800-nm laser light with 120-fs pulse width was subsequently split into two beams, one as the pump beam and another one as the probe beam. The pump beam passed through a harmonic resonator to generate the 400-nm pump beam (the second harmonic of the fundamental 800 nm), whereas the probe beam passed through a sapphire crystal and generated a white-light continuum (400–850 nm). The time-delayed probe beam was controlled by the optical delay rail with a maximum temporal delay at 7000 ps. It would pass through the samples and the signals were then collected by the detector. A reference probe beam was also used to optimize signal-to-noise ratio. The sample solutions were prepared with absorbance approximately to 1.0 at 400 nm and measured in a 2-mm path-length quartz cuvette, and the films were directly fixed on the sample holder. The amorphous solid was mixed with anhydrous KBr, grinded, and squashed into thin plate. The crystal sample was evaporated onto the 25 mm×25 mm×1 mm quartz plate in a saturated solution with different solvents. The consistency of the photophysical properties between the film sample and single crystal sample was confirmed by PL spectra and decay curves (Fig. S8). The spectrometric data were recorded in a 3D wavelength-time-absorbance matrix.

The subtraction of background, the subtraction of scattering light, and chirp correction were done for all the data before analysis. The principal components were ensured by singular value decomposition (SVD), and then the global fitting was carried out with the selected principal components and exponential function using the sequential kinetics scheme based on the fs-TA spectra by Surface Xplorer 4.5. The single-wavelength kinetic fitting was carried out utilized Eq. (2) by Surface Xplorer 4.5.

$$S(t) = e^{-\left(\frac{t-t_0}{t_p}\right)^2} \times \sum_i A_i e^{-\left(\frac{t-t_0}{t_i}\right)} \quad (2)$$

Ns-TA spectroscopy

The ns-TA measurement is based on the EOS pump-probe ns-TA spectrometer system (Ultrafast Systems, USA). The 400-nm pump beam is generated from the femtosecond regenerative amplified Ti:sapphire laser system with similar configuration to fs-TA measurement, while the probe beam is generated from a photonic crystal fiber-based sub-nanosecond pulsed probe light source. It would pass through the samples and the signals were then collected by the detector. A reference probe beam was also used to optimize signal-to-noise ratio. All the sample solutions were tested in a 2 mm path-length cuvette. The spectrometric data were recorded in a 3D wavelength-time-absorbance matrix.

The subtraction of background and scattering light were done for all the data before analysis. The principal components were ensured by singular value decomposition (SVD), and then the global fitting was carried out with the selected principal components and exponential function using the sequential kinetics scheme based on the fs-TA spectra by Surface Xplorer 4.5.

Theoretical calculations

The minimal-energy geometry of single-molecular F-AQ in S_0, S_1, T_1, and T_2 state were optimized by *Gaussian 16* package based on B3LYP-D3/6-311 G(d,p) level. The minimal-energy geometry of the cry-YG and *cry-O* for F-AQ in S_0, S_1, T_1, and T_2 state were optimized by *Gaussian 16* package using the QM/MM method. Clusters constructed from the dimer of F-AQ and the surrounded molecules were extracted from the crystal structure of cry-YG and cry-O. The ONIOM high layer included the central dimer highlighted, was calculated based on B3LYP-D3/6-311 G(d,p) level, while the ONIOM low layer included the molecules surrounded by the central dimer, which was calculated using the UFF (Fig. S13). The vertical absorption energy of the minimal-energy geometries in S_0 state, vertical emission energy of the minimal-energy geometries in S_1, T_1, and T_2 state, and the spin-orbital coupling matrix element (SOCME) were calculated by *ORCA 5.0.3* based on B3LYP-D3/6-311 G(d,p) level. The electron-hole distribution was calculated by *Multifwn 3.8*, and the depiction was conducted by *VMD*. The Hirshfeld surface analysis was performed by *Multifwn 3.8*, and the depiction was conducted by *VMD*.

Data availability

The data generated in this study are provided in the paper, the Supplementary Information and the Source Data file. Source data and the atomic coordinates of the optimized computational models are provided with this paper. The X-ray crystallographic coordinates for structures reported in this study have been deposited at the Cambridge Crystallographic Data Centre (CCDC), under deposition numbers 2407460 (cry-YG) and 2407461 (cry-O). These data can be obtained free of charge from The Cambridge Crystallographic Data Centre via www.ccdc.cam.ac.uk/data_request/cif. Source data are provided with this paper.

References

1. Han, P. et al. Non-doped blue aiegen-based OLED with EQE approaching 10.3 %. *Angew. Chem. Int. Ed.* **62**, e202310388 (2023).
2. Luo, W. et al. Blue TADF conjugated polymers with multi-resonance feature toward solution-processable narrowband blue OLEDs. *Adv. Funct. Mater.* **34**, 2310042 (2024).
3. Suresh, S. M. et al. Judicious heteroatom doping produces high-performance deep-blue/near-uv multiresonant thermally activated delayed fluorescence OLEDs. *Adv. Mater.* **35**, 2300997 (2023).
4. Roberts, M. E. et al. Water-stable organic transistors and their application in chemical and biological sensors. *Proc. Natl Acad. Sci. Usa.* **105**, 12134–12139 (2008).
5. Song, J. et al. Influence of bioreceptor layer structure on myelin basic protein detection using organic field effect transistor-based biosensors. *Adv. Funct. Mater.* **28**, 1802605 (2018).
6. Wang, X. et al. Ultrastable N-type semiconducting fiber organic electrochemical transistors for highly sensitive biosensors. *Adv. Mater.* **36**, 2400287 (2024).
7. Zang, Y. et al. Specific and reproducible gas sensors utilizing gas-phase chemical reaction on organic transistors. *Adv. Mater.* **26**, 2862–2867 (2014).
8. Deng, Z. et al. Insights into the photodynamics of fluorescence emission and singlet oxygen generation of fluorogen activating protein-malachite green systems. *Chem. - Eur. J.* **29**, e202203684 (2023).
9. Fan, Y. et al. Mobile phone flashlight-excited red afterglow bioimaging. *Adv. Mater.* **34**, 2201280 (2022).
10. Li, L. et al. Symmetry-breaking malachite green as a near-infrared light-activated fluorogenic photosensitizer for RNA proximity labeling. *Nucleic Acids Res.* **52**, e36–e36 (2024).
11. Zhao, Y. et al. Fused-ring pyrrole-based near-infrared emissive organic rtp material for persistent afterglow bioimaging. *Angew. Chem. Int. Ed.* **63**, e202317431 (2024).
12. Qiao, W. et al. Naphthyl substituted impurities induce efficient room temperature phosphorescence. *Angew. Chem. Int. Ed.* **62**, e202315911 (2023).
13. Xu, W. et al. Nucleic-acid-base photofunctional cocrystal for information security and antimicrobial applications. *Nat. Commun.* **15**, 2561 (2024).
14. Wu, X. et al. Fabrication of circularly polarized MR-TADF emitters with asymmetrical peripheral-lock enhancing helical b/n-doped nanographenes. *Adv. Mater.* **34**, 2105080 (2022).
15. Wu, X. et al. The role of host–guest interactions in organic emitters employing MR-TADF. *Nat. Photonics* **15**, 780–786 (2021).
16. Zhang, Q. et al. Anthraquinone-based intramolecular charge-transfer compounds: computational molecular design, thermally activated delayed fluorescence, and highly efficient red electroluminescence. *J. Am. Chem. Soc.* **136**, 18070–18081 (2014).
17. Zhang, Q. et al. Design of efficient thermally activated delayed fluorescence materials for pure blue organic light emitting diodes. *J. Am. Chem. Soc.* **134**, 14706–14709 (2012).
18. Chen, J. et al. Robust luminescent molecules with high-level reverse intersystem crossing for efficient near ultraviolet organic light-emitting diodes. *Angew. Chem. Int. Ed.* **61**, e202116810 (2022).
19. Du, S. et al. Hot-exciton mechanism and aie effect boost the performance of deep-red emitters in non-doped OLEDs. *Adv. Mater.* **35**, 2303304 (2023).
20. Lin, C. et al. Efficiency breakthrough of fluorescence OLEDs by the strategic management of “hot excitons” at highly lying excitation triplet energy levels. *Adv. Funct. Mater.* **31**, 2106912 (2021).
21. Liu, F. et al. Anthracene-based emitters for highly efficient deep blue organic light-emitting diodes with narrow emission spectrum. *Chem. Eng. J.* **426**, 131351 (2021).

22. Luo, Y. et al. Ultra-fast triplet-triplet-annihilation-mediated high-lying reverse intersystem crossing triggered by participation of nπ*-featured excited states. *Nat. Commun.* **13**, 6892 (2022).
23. Xu, Y., Xu, P., Hu, D. & Ma, Y. Recent progress in hot exciton materials for organic light-emitting diodes. *Chem. Soc. Rev.* **50**, 1030–1069 (2021).
24. Zheng, Y. et al. Bipolar molecules with hybridized local and charge-transfer state for highly efficient deep-blue organic light-emitting diodes with EQE of 7.4% and CIEy ~ 0.05. *Adv. Opt. Mater.* **9**, 2100965 (2021).
25. Liu, R., Gao, X., Barbatti, M., Jiang, J. & Zhang, G. Promoting intersystem crossing of a fluorescent molecule via single functional group modification. *J. Phys. Chem. Lett.* **10**, 1388–1393 (2019).
26. Liu, Z. et al. Through-space charge transfer within single-component organic crystal: visual detection and rational regulation. *J. Mater. Chem. C.* **12**, 4835–4841 (2024).
27. Zhang, J. et al. Secondary through-space interactions facilitated single-molecule white-light emission from clusteroluminogens. *Nat. Commun.* **13**, 3492 (2022).
28. Xie, F.-M. et al. A dislocated twin-locking acceptor-donor-acceptor configuration for efficient delayed fluorescence with multiple through-space charge transfer. *Angew. Chem. Int. Ed.* **61**, e202213823 (2022).
29. Huang, T. et al. Simultaneously enhanced reverse intersystem crossing and radiative decay in thermally activated delayed fluorophors with multiple through-space charge transfers. *Angew. Chem. Int. Ed.* **60**, 23771–23776 (2021).
30. Yang, S.-Y. et al. Circularly polarized thermally activated delayed fluorescence emitters in through-space charge transfer on asymmetric spiro skeletons. *J. Am. Chem. Soc.* **142**, 17756–17765 (2020).
31. Liang, H. et al. Novel photocatalyst based on through-space charge transfer induced intersystem crossing enables rapid and efficient polymerization under low-power excitation light. *Angew. Chem. Int. Ed.* **63**, e202402774 (2024).
32. Wang, Y. et al. Observation of reverse intersystem-crossing from the upper-level triplet to lowest singlet excitons (t2→s1) in tetra(t-butyl)rubrene-based oleds for enhanced light-emission. *Adv. Funct. Mater.* **32**, 2202882 (2022).
33. Mo, H.-W. et al. Tunable OLEDs: color tuning of avobenzone boron difluoride as an emitter to achieve full-color emission (Adv. Funct. Mater. 37/2016). *Adv. Funct. Mater.* **26**, 6847–6847 (2016).
34. Wang, X. et al. π-stacked donor–acceptor dendrimers for highly efficient white electroluminescence. *Angew. Chem. Int. Ed.* **60**, 16585–16593 (2021).
35. Wang, J.-X. et al. Time-dependent afterglow color in a single-component organic molecular crystal. *Angew. Chem. Int. Ed.* **59**, 10032–10036 (2020).
36. Li, W. et al. Selective expression of chromophores in a single molecule: soft organic crystals exhibiting full-colour tunability and dynamic triplet-exciton behaviours. *Angew. Chem. Int. Ed.* **59**, 3739–3745 (2020).
37. Huang, B. et al. Manipulation of molecular aggregation states to realize polymorphism, AIE, MCL, and TADF in a single molecule. *Angew. Chem. Int. Ed.* **57**, 12473–12477 (2018).
38. Das, G. et al. Fluorescence turn on amine detection in a cationic covalent organic framework. *Nat. Commun.* **13**, 3904 (2022).
39. Liao, R. et al. Approaching an adjustable organic thermochromic luminophore library via the synergistic effects between structure-related molecular dynamics and aggregation-related luminescence. *J. Mater. Chem. C.* **8**, 8430–8439 (2020).
40. Canasa, P. et al. Piezochromic behavior of 2,4,6-triphenylpyrylium tetrachloroferrate. *Small Sci.* **4**, 2400106 (2024).
41. Man, Z. et al. Highly sensitive and easily recoverable excitonic piezochromic fluorescent materials for haptic sensors and anti-counterfeiting applications. *Adv. Funct. Mater.* **30**, 2000105 (2020).
42. Zhai, C. et al. Molecular insertion regulates the donor-acceptor interactions in cocrystals for the design of piezochromic luminescent materials. *Nat. Commun.* **12**, 4084 (2021).
43. Huang, H. et al. Precise molecular design for BN-modified polycyclic aromatic hydrocarbons toward mechanochromic materials. *J. Mater. Chem. A* **8**, 22023–22031 (2020).
44. Li, W. et al. Alkyl Chain Introduction: In Situ Solar-Renewable Colorful Organic Mechanoluminescence Materials. *Angew. Chem. Int. Ed.* **57**, 12727–12732 (2018).
45. Xue, S., Li, M., Han, Y. & Chen, Y. Mechanochromic luminescence from N,O-Chelated diphenylborinates. *Dyes Pigm* **193**, 109484 (2021).
46. Zhang, X., Chi, Z., Zhang, Y., Liu, S. & Xu, J. Recent advances in mechanochromic luminescent metal complexes. *J. Mater. Chem. C.* **1**, 3376–3390 (2013).
47. Qiu, X. et al. Novel 9,9-dimethylfluorene-bridged D–π–A-type fluorophores with a hybridized local and charge-transfer excited state for deep-blue electroluminescence with CIEy ~ 0.05. *J. Mater. Chem. C.* **7**, 592–600 (2019).
48. Qiu, Y., Du, L., Cady, S. D., Phillips, D. L. & Winter, A. H. Optical and EPR detection of a triplet ground state phenyl nitrenium ion. *J. Am. Chem. Soc.* **146**, 10679–10686 (2024).
49. Wang, C., Deng, Z., Phillips, D. L. & Liu, J. Extension of non-alternant nanographenes containing nitrogen-doped stone-thrower-wales defects. *Angew. Chem. Int. Ed.* **62**, e202306890 (2023).
50. Zhuang, W. et al. Synthesis, structures, and chiroptical properties of nbn-doped helicenes with boron atoms in the inner rims. *Precis. Chem.* **2**, 28–39 (2024).
51. Gaussian 16 Rev. C.01 (Wallingford, CT, 2016).
52. Neese, F., Wennmohs, F., Becker, U. & Riplinger, C. The ORCA quantum chemistry program package. *J. Chem. Phys.* **152**, 224108 (2020).
53. Humphrey, W., Dalke, A. & Schulten, K. VMD: visual molecular dynamics. *J. Mol. Graph.* **14**, 33–38 (1996).
54. Lu, T. & Chen, F. Multiwfn: a multifunctional wavefunction analyzer. *J. Comput. Chem.* **33**, 580–592 (2012).
55. Huang, G. et al. Room-temperature stable noncovalent charge-transfer dianion biradical to produce singlet oxygen by visible or near-infrared light photoexcitation. *J. Phys. Chem. Lett.* **12**, 4306–4312 (2021).
56. Nocera, G. et al. Electron transfer reactions: kotbu (but not naotbu) photoreduces benzophenone under activation by visible light. *J. Am. Chem. Soc.* **140**, 9751–9757 (2018).

Acknowledgements

This work was supported by grants from the Hong Kong Research Grants Council (GRF 17316922), The University of Hong Kong Development Fund 2013-2014 project "New Ultrafast Spectroscopy Experiments for Shared Facilities", Major Program of Guangdong Basic and Applied Research (2019B030302009), Guangdong-Hong Kong-Macao Joint Laboratory of Optoelectronic and Magnetic Functional Materials (2019B121205002) and Key-Area Research and Development Program of Guangdong Province (2020B0101370003).

Author contributions

Z.D. and D.P. conceived the study. Z.D. synthesized the molecule, fabricated different solid states, and performed the spectroscopic study. C.H. was responsible for the application relevant work. Y.L. carried out the transient emission spectroscopy. and phosphorescence spectroscopy. J.H. performed the PXRD experiments. L.L. conducted the

fluorescence QY measurement. X.P. carried out the SC-XRD measurement. Z.D., G.H., and D.P. discussed the results and edited the manuscript.

Competing interests
The authors declare no competing interests.

Additional information
Supplementary information The online version contains supplementary material available at https://doi.org/10.1038/s41467-024-55569-0.

Correspondence and requests for materials should be addressed to David Lee Phillips.

Peer review information *Nature Communications* thanks Koichi Iwata and the other, anonymous, reviewers for their contribution to the peer review of this work. A peer review file is available.

Reprints and permissions information is available at http://www.nature.com/reprints

Publisher's note Springer Nature remains neutral with regard to jurisdictional claims in published maps and institutional affiliations.

Open Access This article is licensed under a Creative Commons Attribution-NonCommercial-NoDerivatives 4.0 International License, which permits any non-commercial use, sharing, distribution and reproduction in any medium or format, as long as you give appropriate credit to the original author(s) and the source, provide a link to the Creative Commons licence, and indicate if you modified the licensed material. You do not have permission under this licence to share adapted material derived from this article or parts of it. The images or other third party material in this article are included in the article's Creative Commons licence, unless indicated otherwise in a credit line to the material. If material is not included in the article's Creative Commons licence and your intended use is not permitted by statutory regulation or exceeds the permitted use, you will need to obtain permission directly from the copyright holder. To view a copy of this licence, visit http://creativecommons.org/licenses/by-nc-nd/4.0/.

© The Author(s) 2024